Characterization of divertor footprints and the pedestal plasmas in the presence of applied $n = 3$ fields for the attached and detached conditions in NSTX

2014 Plasma Phys. Control. Fusion 56 015005

(http://iopscience.iop.org/0741-3335/56/1/015005)

IOP Publishing Plasma Physics and Controlled Fusion

Plasma Phys. Control. Fusion **56** (2014) 015005 (10pp) doi:10.1088/0741-3335/56/1/015005

Characterization of divertor footprints and the pedestal plasmas in the presence of applied $n = 3$ fields for the attached and detached conditions in NSTX

J-W Ahn[1], F Scotti[2], K Kim[2], J M Canik[1], J D Lore[1], R Maingi[1], A G McLean[3], R E Bell[2], A Diallo[2], S P Gerhardt[2], T K Gray[1], S M Kaye[2], B P LeBlanc[2], V A Soukhanovskii[3] and K Tritz[4]

[1] Oak Ridge National Laboratory, Oak Ridge, TN, USA
[2] Princeton Plasma Physics Laboratory, Princeton, NJ, USA
[3] Lawrence Livermore National Laboratory, Livermore, CA, USA
[4] Department of Physics and Astronomy, John's Hopkins University, Baltimore, MD, USA

E-mail: jahn@pppl.gov

Received 23 July 2013, revised 6 November 2013
Accepted for publication 18 November 2013
Published 10 December 2013

Abstract

Recent progress in the study of 3D field effects on the divertor and pedestal plasmas is reported with the use of a new set of diagnostics. A wide angle visible camera provides 2D data of lower divertor surface covering almost the full range of radius (r) and toroidal angle (Φ), a significant advantage over the conventional 1D radial profile in examining non-axisymmetric effects of 3D fields on the divertor footprints. The spatial distribution of connection lengths (L_c) calculated by vacuum field line tracing in the presence of 3D fields ($n = 3$) agrees with the footprint pattern observed in the 2D wide angle camera images. The full (r, Φ) image data with high temporal resolution revealed that the spatial structure of modified divertor footprints is maintained even during the edge-localized modes (ELMs) triggered by applied $n = 3$ fields, when the ELM size is sufficiently small, i.e. the ELMs are 'phase locked' to the imposed perturbation field structure. This phase-lock is lost during the ELM rise time for ELMs with large energy loss, e.g. $\Delta W_{ELM}/W_{MHD} > 4$–5%. Divertor gas puff was used to create detached divertor condition and the effect of 3D fields on the detachment was investigated. The divertor remains partially detached with the 3D field application when a sufficient amount of gas is injected into the divertor region, which is accompanied by a noticeable drop of pedestal electron temperature (T_e). However, with a lower gas puff, the divertor plasma re-attaches, when 3D fields were applied to the detached plasma, and the pedestal T_e rises back up. There observed no other change in the pedestal profile associated with the re-attachment, indicating that this is likely to be dominated by a change in the electron thermal transport processes. A TRANSP analysis shows that the drop of pedestal electron heat diffusivity (χ_e) is responsible for this change but the source of this reduction is yet unclear.

Keywords: 3D fields, non-axisymmetric effect, detachment, divertor profile and footprints, pedestal profiles

(Some figures may appear in colour only in the online journal)

1. Introduction

Since pioneered at DIII-D [1, 2], externally imposed non-axisymmetric, i.e. 3D, magnetic perturbation fields have been found to suppress or mitigate edge-localized modes (ELMs) at several other tokamaks such as JET [3], ASDEX-U [4] and KSTAR [5]. They have been also found to trigger ELMs in the lithium enhanced ELM-free plasmas at NSTX [6, 7]. The addition of 3D fields in tokamak plasmas changes the magnetic topology, causing pronounced lobes to form near the separatrix X-point. This leads to the 'strike point splitting' and divertor flux striations [8], as observed in experiments [9–12]. This strike point splitting produces multiple local peaks and valleys in the 1D divertor heat and particle flux profiles. The heat and particle flux footprints in NSTX have been confirmed to be consistent with vacuum field line tracing (FLT) of the superposition of vacuum 3D fields ($n = 3$, n being the toroidal mode number) and 2D equilibrium fields [11, 12]. The inclusion of the response of the plasma inside the separatrix, calculated with the Ideal Perturbed Equilibrium Code (IPEC) [13], as the base equilibrium for FLT did not alter [12] the computed structure of striations significantly compared to the vacuum modeling. Heat flux profiles for the ELMs triggered by applied 3D fields ($n = 3$) were measured with a fast infrared (IR) camera [14, 15] and appear to be phase locked to the $n = 3$ field structure [12], as also reported in DIII-D experiments [9, 10]. The 3D field effects on the divertor footprints have been so far examined using 1D profiles at a specific toroidal location and a more comprehensive investigation with 2D profiles is desired. We will present the first 2D results obtained from a wide angle visible camera in this paper.

While the so-called density pump-out (decrease of line average electron density) is often observed for 3D fields application experiments in other tokamaks, which is attributed to the decrease of pedestal density [16, 17] by 3D fields, it is generally not observed in NSTX; the line average density evolution is unaffected. With carbon plasma facing components (PFC), the pedestal electron temperature rises when the 3D fields are applied, leading to the higher pedestal pressure gradient [6, 7]. However, when the PFC surface is coated with lithium, a flat spot is observed for the region $\Psi_N \sim 0.8$–0.9 in both the electron density and temperature with the application of 3D fields [18]. The mechanism by which these changes to the pedestal profiles are induced by 3D fields, and the relation to the ELM stability are yet to be understood.

Applied 3D fields are being considered for ITER for ELM suppression because of their success in present day tokamaks. However, this type of operating scenario must be compatible with the divertor partial detachment necessary for the heat flux mitigation. Results from NSTX [12] showed that partially detached divertor plasma can re-attach by the applied 3D fields ($n = 3$), but this can be avoided when the detachment is enhanced by puffing sufficient amount of gas into the divertor region. This investigation is more difficult in other devices where the density pump-out causes low line average density during the 3D field application. As there is no density pump-out in NSTX, the divertor density can be raised more easily to achieve divertor detachment, and the impact of 3D fields on detachment has been investigated in detail.

Section 2 will describe the diagnostic techniques used in this work. The impact of 3D fields on the divertor plasma is discussed in section 3. Results for the divertor detachment and 3D fields for both the divertor and pedestal plasmas will be given in section 4. A review of the 3D field effect on the pedestal profiles in the attached regime will be also included in this section. Section 5 is dedicated to the summary and discussion.

2. Diagnostics

NSTX routinely uses lithium coating on the PFC surface to generate ELM-free H-mode plasmas [19], for which the reduced recycling coefficient due to the lithium coating leads to the relaxation of the density profile that keeps the plasma in the peeling–ballooning stable region [20–22]. However, lithium coating changes the PFC surface emissivity and complicates interpretation of IR photon flux for the surface temperature measurement. To overcome this issue, a dual band adaptor has been developed [15] for the existing high speed IR camera [14]. The adaptor uses a long-wave pass dichroic beam splitter which efficiently separates mid-wavelength band IR (MWIR, 4–6 μm) and long-wavelength band IR (LWIR, 7–10 μm) photons. Then the ratio of measured radiant energy in the two IR wavelength regions is used to obtain the divertor surface temperature. This technique has the advantage of being mostly independent of surface emissivity [15]. The entire system provides the spatial and temporal resolution of ~0.7 cm and 1.6 kHz. Surface temperature data for the work in this paper are all from the dual band IR measurement and the calculation of heat flux is conducted using a 2D heat conduction solver, THEODOR [23]. The effect of top surface layer is taken into account by introducing a heat transmission coefficient, α, in the THEODOR data analysis. $\alpha = 10$–$15\,\mathrm{kW\,m^{-2}\,K^{-1}}$ was used in this work to avoid negative heat flux in the inter-ELM period. Figure 1 shows the plasma poloidal cross section with the location of other relevant diagnostics overlaid.

Two wide angle visible cameras have been recently implemented [24] in NSTX. Each of these has a capability of covering nearly full toroidal angle at the lower divertor surface. The plasma is imaged through an interference filter selected from a filter wheel; we find that the Li I (670.9 nm) filter usually provides the best data to resolve fine structures of divertor footprints. The brightness measurement from these cameras represents the line integral of the Li I emissivity which is usually limited to the region in very proximity to the target surface. For typical divertor electron temperatures (T_e) and densities (n_e) in the NSTX divertor, it can be assumed that the majority of the photons come from excitation events. Local Li I emissivity is then given by $E_{\mathrm{Li\,I}} = n_{\mathrm{Li}} \times n_e \times \mathrm{PEC}_{\mathrm{ex}}(T_e, n_e)$, where the photon emission coefficient (PEC) for excitation has a non-negligible dependence on the local T_e and n_e. Other source of toroidal asymmetries includes asymmetries in n_e and n_{Li}. Toroidal asymmetries in n_{Li} can arise as a result of the toroidally asymmetric lithium deposition profile (as a result of the Li deposition pattern from two lithium evaporators from the

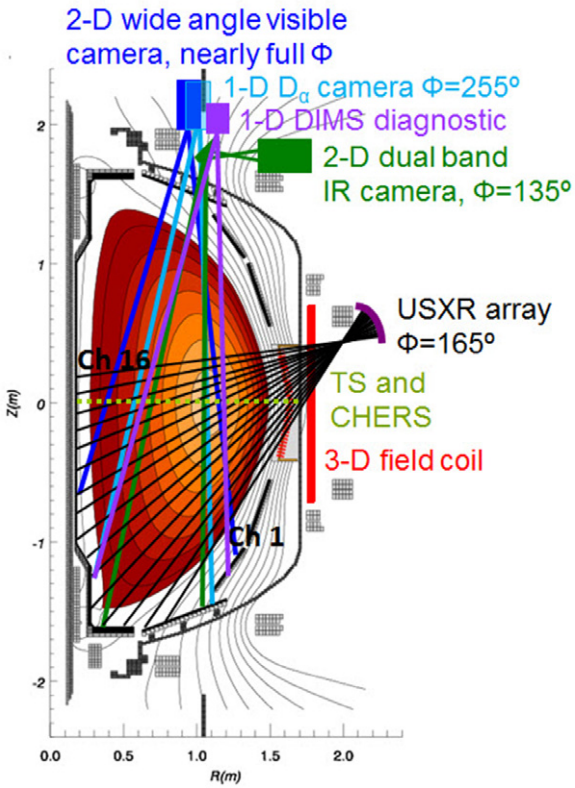

Figure 1. Poloidal cross section of an NSTX plasma with relevant diagnostics overlaid. The toroidal location (Φ) of camera diagnostics are indicated as well as the poloidal chords of USXR diagnostic.

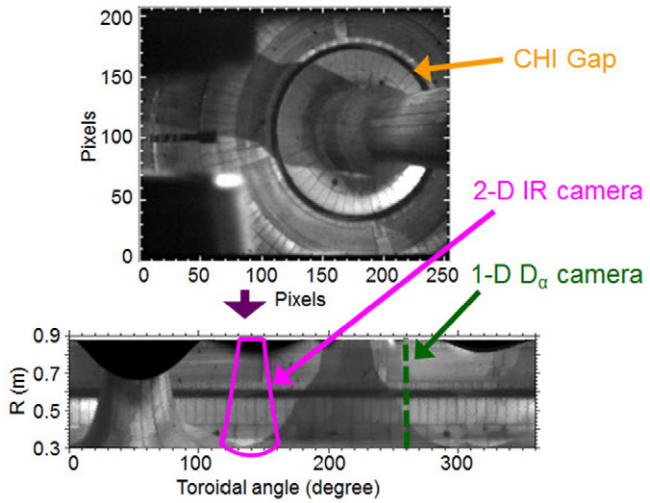

Figure 2. A raw image from the wide angle visible camera (upper) and the re-mapped image (lower) from the (x, y) to (r, Φ) plane. The coverage by the 2D dual band IR camera and the 1D D_α camera are also indicated in the corresponding toroidal locations.

top of the machine, which are toroidally separated by 150°), and as a result of toroidal asymmetries in lithium sputtering yield which by itself is dependent on the local T_e and target surface temperature. The frame speed of the wide angle visible camera is typically 10–20 kHz and the spatial resolution is ~0.8 cm. An example image with 256 × 208 pixels from one of the two cameras is given in figure 2. This image is re-mapped to the plot in the radius (r) and toroidal angle (Φ) plane, which shows the helical heat deposition pattern more clearly and makes the comparison with modeling significantly easier.

The toroidal and radial coverage of the 2D dual band IR camera and the 1D D_α camera [25] is overlaid in figure 2 as well. Note that the D_α camera is toroidally displaced from the IR camera by 120°, which is the same period as to the one produced by the $n = 3$ magnetic perturbation fields.

A newly installed 1D ultraviolet–visible–near infrared (UV–VIS–NIR) divertor imaging spectrometer (DIMS) with a total of 19 poloidal chords (centimeter-scale spatial resolution) to cover the lower divertor area [26] was also used to monitor high-n Balmer line emission intensities, see figure 1. This is particularly useful to check volume recombination in the divertor area, which is a typical indicative of radiative/detached divertor condition.

Also indicated in figure 1 are the poloidal lines of sight of the ultra-soft x-ray (USXR) diagnostic [27] that are located at the toroidal angle of 165° and view the lower half of the plasma cross section. Although these poloidal, line-integrated measurements do not specify the radial profile of USXR emission, the poloidal coverage can provide information about the localized emission. Because the SXR emission intensity depends both on the electron temperature and density, these measurements can provide information to infer the local plasma conditions. The USXR diagnostic was operated with a 5 μm Be filter for work in this paper, which filters out the low energy emission from the edge plasma and SOL and provides a fast measurement of SXR intensity from the mid-pedestal region to the plasma core. The pedestal SXR emission can be used to monitor the effects of ELMs and imposed 3D fields on the local plasma on fast time scales (500 kHz). The mid-plane electron temperature (T_e) and density (n_e) profiles are measured by the Thomson scattering (TS) [28] and the charge exchange recombination spectroscopy (CHERS) diagnostic [29] provides the mid-plane ion temperature (T_i) and toroidal velocity (V_t) profiles.

3. Effect of 3D fields on divertor plasma

The applied 3D fields interact with the background 2D equilibrium field and generate 3D topology of perturbed field lines in the plasma edge. The boundary plasma therefore is no longer in the nested flux surface structure and becomes stochastic. The poloidal magnetic flux is organized by complex topological structures known as homoclinic tangles [30]. These tangles can intersect with the divertor surface and cause an apparent 'splitting' of the strike point, which modifies the divertor heat and particle flux profiles. Plots of field line vector at the mid-plane when $n = 1$ or $n = 3$ perturbations are applied are shown in figures 3(a) and (b). A poloidal cross section of Poincaré plot using the vacuum FLT for $n = 3$ case is shown in figure 3(c), where the stochastic magnetic field layer in the boundary region and unstable separatrix manifolds are visible. Data presented in this paper are primarily in the absence of ELMs, i.e. either the applied 3D fields did not trigger an ELM

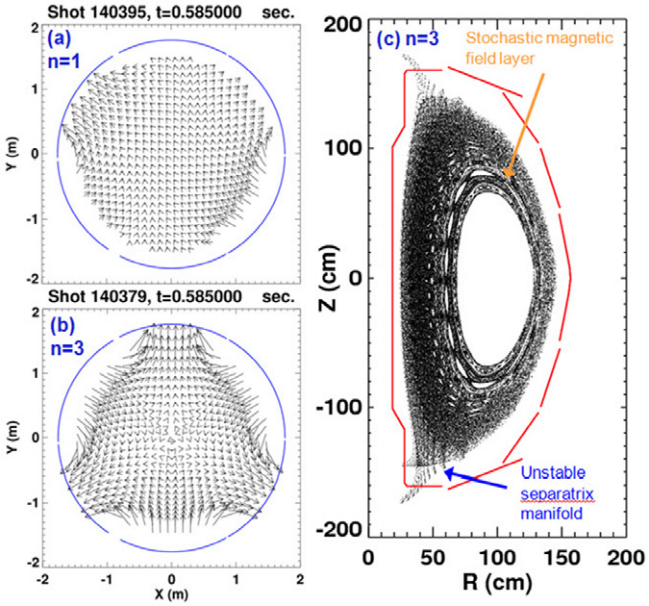

Figure 3. Field line vector at the mid-plane of NSTX, viewed from the top of the machine, when (*a*) $n = 1$ and (*b*) $n = 3$ perturbation fields are applied. The poloidal cross section of Poincaré plot for $n = 3$ using the vacuum FLT is shown in (*c*).

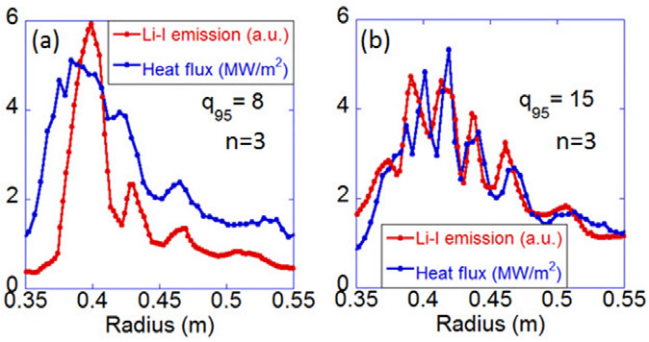

Figure 4. Comparison of 1D radial profiles of heat flux (blue) and Li I ($\lambda = 670.9$ nm) emission intensity (red), averaged over data with toroidal angles (Φ) between 141° and 146°, with $n = 3$ magnetic perturbations applied. (*a*) is for lower q_{95} (= 8) and (*b*) is for higher q_{95} (= 15).

or data was taken before an ELM was triggered, except the data of divertor footprints caused by 3D field triggered ELMs described in section 3.2.

3.1. Use of full 2D visible image data and comparison with 1D heat flux profile

As the divertor footprints become non-axisymmetric with the application of 3D fields, investigation of spatial structure of divertor heat and particle deposition requires profile data from multiple toroidal locations for more comprehensive study. Although traditional 1D radial flux profiles are still useful, a 2D image at the divertor surface covering a wide range of radius and toroidal angle facilitates easier identification of asymmetric divertor flux deposition. This also makes the comparison with modeling much easier. Figure 4 shows comparison of radial heat flux and Li I emission intensity

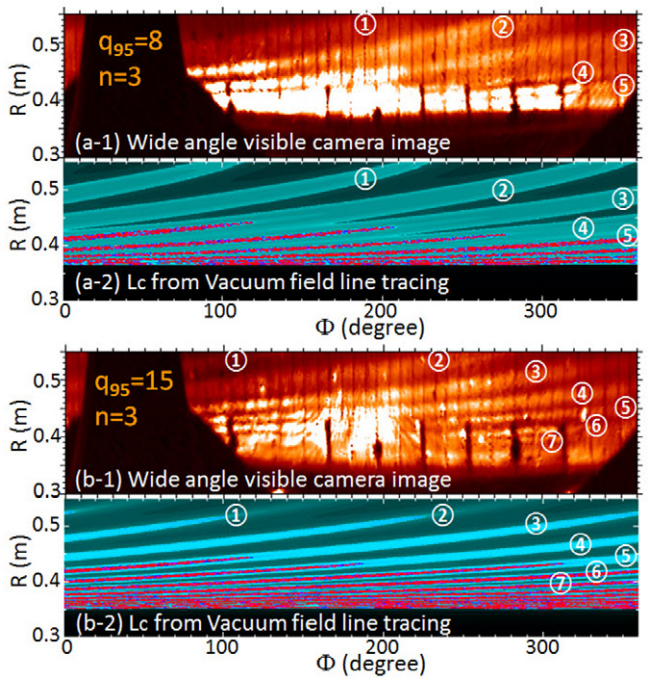

Figure 5. Comparison of 2D wide angle visible camera image (Li I, $\lambda = 670.9$ nm) of lower divertor area in NSTX to the contour plot of connection lengths (L_c) calculated from vacuum FLT, with $n = 3$ magnetic perturbations applied. (*a*) is for a lower q_{95} (= 8) case and (*b*) for a higher q_{95} (= 15). For each of (*a*) and (*b*), identified striations induced by applied $n = 3$ fields are indicated by circled numbers in the camera image and in the L_c contour plot. The visible camera images are re-mapped from (x, y) to (r, Φ) plane. The dark portion on the left hand side in each image represents the center column.

profiles, measured and averaged over data for toroidal angles ranging from 141° to 146°, in the presence of $n = 3$ magnetic perturbations. Figure 4(*a*) is for a lower q_{95} (~8) plasma and figure 4(*b*) is for a higher q_{95} (~15) case. It is clearly seen that the pattern of strike point splitting by $n = 3$ fields has strong dependence on q_{95}, i.e. more and finer local peaks and valleys are observed for higher q_{95}. Note that the radial location of local peaks induced by 3D fields is in reasonably good agreement between the heat flux and Li I emission intensity profiles. This is interesting because Li I brightness is not a direct representation of heat flux, and this similarity suggests a comparable profile of the impinging heat flux and the surface Li I excitation. The re-mapped raw image from the wide angle visible camera through Li I filter is compared to the contour plot of connection lengths (L_c) in (r, Φ) plane, calculated by vacuum FLT, in figure 5. Again, comparison was made for both high and low q_{95} cases as was in figure 4. The 2D wide angle camera images show multiple striations helically distributed across the divertor surface that were caused by homoclinic tangles induced by externally applied $n = 3$ magnetic perturbations and individual striations are indicated by circled numbers to be compared to those in the vacuum FLT plot. The vacuum FLT calculation was done by superimposing $n = 3$ non-axisymmetric perturbation fields onto the 2D axisymmetric equilibrium fields. Also included in the calculation was the contribution of intrinsic error fields ($n = 1$ and $n = 3$ components from the non-circularity of

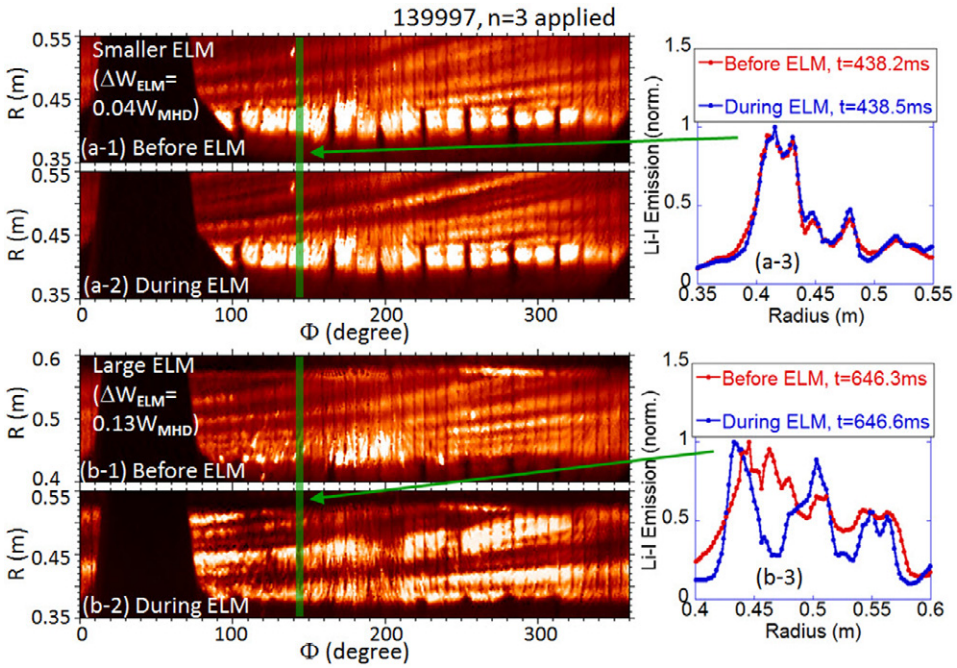

Figure 6. Images of wide angle visible (Li I, $\lambda = 670.9$ nm) camera before ((*a*-1) and (*b*-1)) and during ((*a*-2) and (*b*-2)) the ELM, with the application of $n = 3$ magnetic perturbations. Pictures of (*a*) were for a smaller size ELM and (*b*) for a large ELM. (*a*-3) and (*b*-3) are comparison of normalized 1D radial Li I emission profiles before and during the ELM, averaged over data with toroidal angles (Φ) between 141° and 146° (indicated as a green bar), respectively for a smaller and large ELM. The images are re-mapped from (x, y) to (r, Φ) plane. The dark portion on the left hand side in each image represents the center column. The scale of light intensity for the ELM case, images (*a*-2) and (*b*-2), was adjusted for clearer comparison with the before ELM case.

the PF5 coil and the $n = 1$ component from the TF coil, as described in [31]). For example, the coil current for the $n = 3$ error field correction (EFC) is about 200 A and the current for $n = 3$ perturbation in this work is about −500 A. Therefore, the error field contribution is obviously non-negligible and should be properly taken into account in the FLT calculation. It is shown that the more and finer striations observed in the camera image in the high q_{95} case (figure 5(*b*-1)) are well reproduced in the L_c contour plot (figure 5(*b*-2)). Low q_{95} case (figures 5(*a*-1) and (*a*-2)) produces less and wider striations in both the image data and the L_c contour plot. Another important result is that specific spatial structures of these striations from the vacuum FLT are in good agreement with the camera image; the overall radial and toroidal variation of L_c represents the observed spatial distribution of Li I brightness well, although there appears to be slight difference in the toroidal extent of each striation (e.g. by 20°–30° at $r = 55$ cm). Each of the identified striations is number coded in both the camera image and the L_c plot. This agreement confirms the conclusion of previous work [11, 12] that the vacuum FLT reproduces the divertor footprints well in NSTX for the application of $n = 3$ magnetic perturbations. We note the toroidal variation in the thickness of lithium coating due to the geometry of the two lithium evaporators located at the top of NSTX and the shadow effect by the center stack. This produces a background asymmetry and irregularity in the brightness of Li I emission, as mentioned in [24], that is unrelated to the toroidal asymmetry in the divertor flux caused by 3D fields.

3.2. Divertor footprints for triggered ELMs

The transient heat and particle flux during an ELM is recognized as a serious problem because of its potential to damage PFC material. ELM control using the applied 3D fields is sought as a solution; previous studies revealed that the divertor heat flux is 'phase locked' to the applied 3D fields, i.e. the spatial structure of heat flux profile from ELMs triggered by applied 3D fields ($n = 3$) [12], or in the presence of 3D fields [10], follows the imposed perturbation field structure. The plasma would have remained ELM-free without the applied 3D fields. By applying the re-mapping technique of wide angle images for the divertor footprints of the triggered ELMs, we were able to check data with various ELM energy losses triggered by $n = 3$ fields. It is found that the phase locking holds for ELMs with smaller energy loss ($\Delta W_{ELM}/W_{MHD} <$ 4–5%), but the spatial structure of ELM footprints deviates from that of stationary non-axisymmetric footprint pattern in the presence of $n = 3$ fields when the ELM size becomes larger. This is qualitatively similar to the result reported in DIII-D [9]. Figure 6 illustrates an example of a smaller and a large ELM case. 2D footprint pattern before and during a smaller ELM ($\Delta W_{ELM}/W_{MHD} = 4\%$), figures 6(*a*-1) and (*a*-2) respectively, shows excellent agreement for the whole area of divertor surface. Figure 6(*a*-3) compares normalized 1D radial profiles of Li I emission intensity, averaged over data for toroidal angles between 141° and 146° indicated by a green vertical bar in figures 6(*a*-1) and (*a*-2), and a good profile overlap of the two profiles is clearly visible. However, for another ELM with large energy loss ($\Delta W_{ELM}/W_{MHD} = 13\%$)

during the same discharge, the locking is lost (see figures 6(*b*-1) through (*b*-3)). It is easily seen in figure 6(*b*-3) that the two profiles before and during the ELM have local peaks and valleys in different radial locations. Note that the brightness scale of figures 6(*a*-2) and (*b*-2) was adjusted to the level of figures 6(*a*-1) and (*b*-1) for easier direct comparison. The dependence of phase locking on the ELM size has an important implication that some minimal level of ELM mitigation would be necessary in order for the spatial distribution of ELM heat flux with 3D fields to be aligned with the footprint pattern generated by the imposed 3D fields. If this phenomenon is extrapolable to ITER, the ELM energy deposition pattern onto the divertor plates, regulated by the applied 3D fields for a certain level of ELM mitigation, should be taken into account in the design of divertor plates as well as their cooling scheme to avoid localized damage of material surface. For example, dynamic rotation of the applied 3D fields in the toroidal direction will help disperse heat and particle load more evenly.

4. Effect of 3D fields on partial divertor detachment and pedestal profiles

The compact size of the ST geometry naturally leads to more serious heat flux problem for a given heating power and plasma current. This is true for both the steady state and the transient ELM heat deposition. Therefore, the ELM control using the 3D fields and the peak heat flux reduction technique with the divertor detachment must be compatible with each other. Partial divertor detachment both on the inboard and outboard sides has been demonstrated in the high performance H-mode plasmas in NSTX [32]. Results from NSTX have shown that partially detached divertor plasma can be re-attached by applying 3D fields ($n = 3$). However, this can be avoided when the detachment is enhanced by puffing sufficient gas into the divertor region.

4.1. Experimental approach and effect of 3D fields on divertor plasma

Figure 7 shows the time trace of several plasma parameters. A large amount of deuterium (D_2) gas is puffed into the lower divertor area through the 'CHI gap' between the inner and outer divertor plates (see figure 2), for naturally ELMy H-mode plasmas to produce partially detached divertor condition, i.e. detachment only occurs near the strike point. A small amount of lithium (50 mg for the inter-shot evaporation, compared to ~200 mg necessary for the full ELM suppression) was used to condition the PFC surface. The orange shaded period in figure 7 represents the time of D_2 injection. Figure 7(*d*) is the time trace of a 3D coil current. 0.2 kA of $n = 3$ EFC field is applied first and then the $n = 3$ perturbation field is superimposed for the second half of the gas puff period. The amplitude of 3D coil current ($I_{3-D} = -0.5$ kA) is below the ELM triggering threshold that was confirmed from the ELM triggering experiment in the lithium enhanced ELM-free plasma. Plots in figure 8 are the calculated heat flux profile onto the divertor surface during the inter-ELM period, based

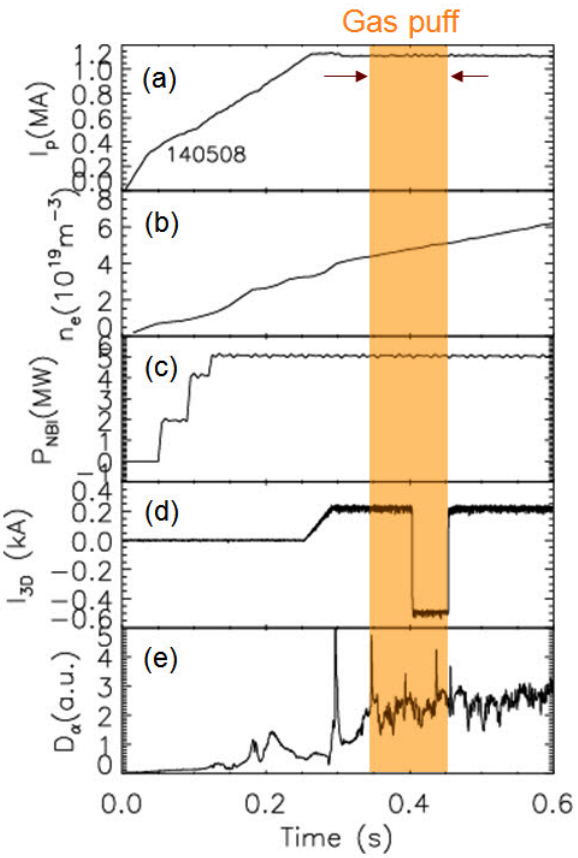

Figure 7. Time trace of (*a*) plasma current, (*b*) line average density, (*c*) NBI power, (*d*) 3D field coil current and (*e*) divertor D_α signal, taken during a divertor detachment and 3D field application experiment. The $n = 3$ perturbation fields are superimposed onto the $n = 3$ error correction fields for the second half ($t = 0.4$–0.45 s) of the detachment period ($t = 0.35$–0.45 s, orange shadow).

on the dual band IR camera data. Two levels of gas amount for the divertor puff were tested. Figure 8(*a*) is for the low gas puff (2000 Torr of pressure, estimated to be $\sim 7 \times 10^{21}$ D s^{-1} of particle flow rate) and (*b*) is for the high gas puff (3000 Torr of pressure, estimated to be $\sim 11 \times 10^{21}$ D s^{-1} of flow rate) case. Heat flux profiles in red are before the gas puff and are peaked near the strike point at $r \sim 38$ cm in both cases, which indicates that the divertor plasma is attached. The blue profiles are obtained after the detachment onset (by gas puff) but before the 3D field application. The peak heat flux is reduced by ~70% (from ~7 MW m^{-2} to ~2 MW m^{-2}) compared to those in the attached condition before the gas puff. It is also seen that the heat flux profile after the detachment onset is slightly higher for the low gas puff case. This is interpreted as a 'weaker' detachment compared to the high gas puff case. The green profiles are after the 3D field was applied to the detachment. It is clearly seen that the heat flux profile becomes peaked again in the low gas puff case; the divertor plasma re-attaches. However, it stays flat in the high gas puff case, which indicates that the plasma remains detached. Therefore, the 3D fields can re-attach weakly detached plasma but this can be avoided by enhancing detachment with higher gas puff.

The evidence of detachment by divertor gas puff and re-attachment induced by the applied 3D fields is also provided by

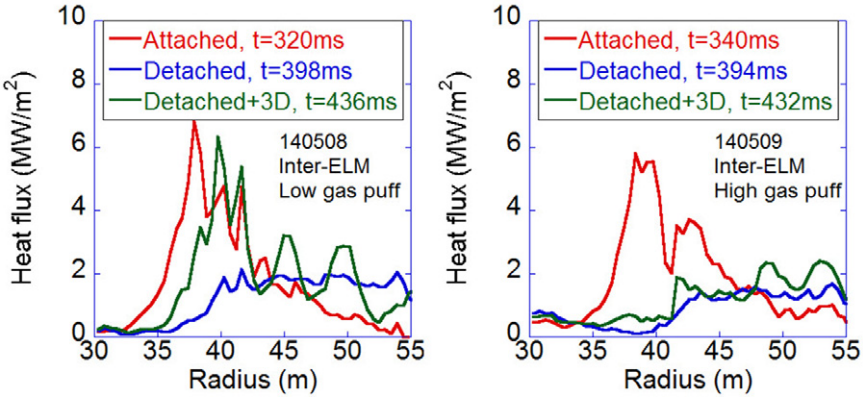

Figure 8. Measured heat flux profiles for discharges with divertor detachment by (*a*) low and (*b*) high divertor gas puff (D_2). Each profile is color coded; red is before gas puff, blue is after gas puff, green is after gas puff plus 3D field application.

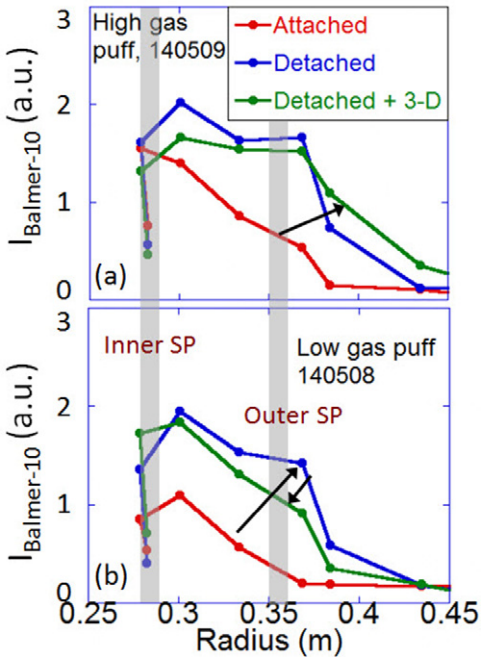

Figure 9. Radial profile of Balmer-10 emission intensity for (*a*) high gas puff and (*b*) low gas puff case. Each plot shows data for three time slices; before gas puff (red, attached), during gas puff (blue, detached), and 3D field applied during gas puff (green, detached + 3D fields). The location of inner and outer strike points (SPs), from EFIT, is shown by the gray vertical bars. The arrows indicate that the profile continues to grow in the (*a*) high gas puff case and the profile reverts with the onset of re-attachment in the (*b*) low gas puff case.

spectroscopic data. High-*n* Balmer line emission, for example Balmer-10, provided by DIMS diagnostic [26] is a good indicative of volume recombination and is only present in the condition of low $T_e (< 5\,\text{eV})$ and high density. We thus use this signal as an indicator of divertor plasma condition. Figure 9 shows the radial distribution of line integrated Balmer-10 line emission intensity for the high and low gas puff cases. The radius values here represent radii of the intersection of poloidal chords of DIMS diagnostic with the divertor surface (see figure 1, where only the first and last poloidal chords are shown for clarify). The location of inner and outer strike points is also overlaid in figure 9. Note that the poloidal chords are line integrated so that data are not only for the strike points but also contain contributions from regions above the divertor surface including the X-point region. The inner strike point almost always detaches in NSTX [32], and this is demonstrated in both figures 9(*a*) and (*b*) that the Balmer-10 intensity near the inner strike point is peaked even before the gas puff stage (the red profiles), while the intensity near the outer strike point remains low. With the gas puff, intensities near the outer strike point rapidly increases, leading to the broadening of the emission profile (blue profiles). This continues to grow after the application of 3D fields in the high gas puff case, figure 9(*a*), but with the onset of re-attachment by 3D fields in the low gas puff case, figure 9(*b*), the process begins to reverse (green profiles). This observation is consistent with the temporal evolution of surface heat flux profiles shown in figure 8.

4.2. Effect on the pedestal plasma

4.2.1. Background study for the attached divertor plasma. This sub-section is intended to review previous NSTX results in the attached condition in comparison with the data in the detached condition to be presented in section 4.2.2. As described in the introduction section, 3D fields not only modify divertor footprints but also change the pedestal profiles in NSTX [6, 7, 18]. However, the effect is less consistent compared to the robust strike point splitting observed in the divertor plasma, as explained below. Comparison of pedestal profiles before and after the 3D fields ($n = 3$) without the use of lithium PFC coating show the increase of T_e gradient by 3D fields while n_e remains almost unchanged. A modified tanh fitting gives ~30% increase in the peak edge pressure gradient (∇p_e) caused by this increase [6, 7]. The increase of ∇p_e was calculated to be sufficient to destabilize peeling–ballooning modes, which is consistent with the triggering of large ELMs observed in NSTX [6]. Note that T_i profile decreases only modestly but the drop of overall V_t profile after $n = 3$ is quite significant.

When lithium coating was used to produce ELM-free H-mode plasmas, however, the effect of the applied 3D fields on the pedestal plasma is not the same as the case without lithium described above. A flattening in both the T_e and n_e

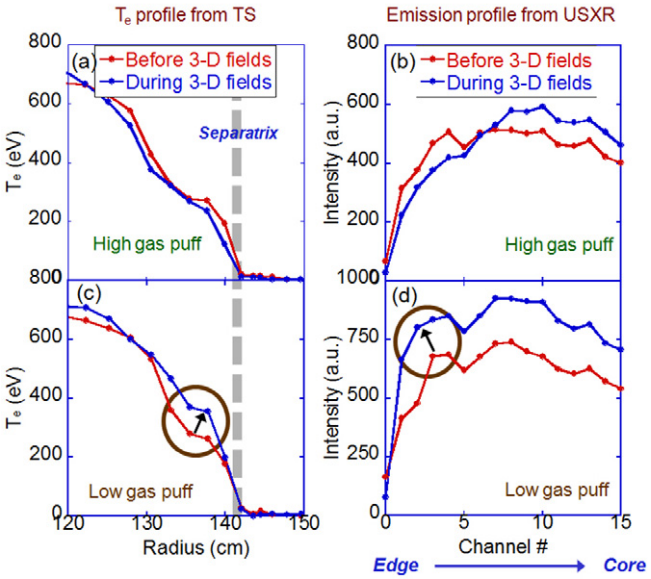

Figure 10. Pedestal T_e profile (left column) and poloidal USXR channel signals (right column, see figure 1). The upper row ((*a*) and (*b*)) is for high gas puff and the lower row ((*c*) and (*d*)) is for the low gas puff, with 3D fields applied later during the detached phase in both cases.

profiles in the region of $\Psi_N \sim 0.8$–0.9 is observed [18], where Ψ_N is the normalized poloidal flux. In other words, the rise of pressure gradient reported in [6, 7] does not occur in this case. However, ELMs are still triggered as a result of edge destabilization after the application of $n = 3$ fields. This suggests that the mechanism of ELM triggering may not be limited to the increase of edge pressure gradient but can be attributed to another cause. The change in the T_i and V_t profiles is similar to that observed in the case of no lithium coating. A FLT from the SIESTA magnetic field modeling [18] was carried out to compare to the experimental observation. The SIESTA code [33] can generate a quasi-resistive equilibrium allowing for the possibility of magnetic island formation. It revealed the magnetic island overlap in the radial region similar to where the flattening of T_e and n_e is observed, i.e. $\Psi_N \sim 0.8$–0.9. However, the electron thermal and particle diffusivity due to stochastic transport using the SIESTA magnetic field are much lower than the values inferred from the SOLPS 2D edge modeling using the observed profile data [18].

4.2.2. Effect on the pedestal plasma with divertor detachment. As the detachment of divertor plasma is established, the pedestal T_e progressively drops with increasing gas puff, while the pedestal n_e changes only little. The T_i and V_t profiles also decrease only modestly in the overall pedestal region with the onset of detachment. Therefore, the pedestal T_e drop is most prominently observed in NSTX when the divertor plasma detaches, which also leads to the reduction of pedestal electron pressure, $p_{e,ped}$. Figure 10 illustrates the effect of 3D fields on the pedestal plasma with detachment. Panels (*a*) and (*c*) are the mid-plane T_e profiles and (*b*) and (*d*) are the emission profiles from the USXR array. The upper row, panels (*a*) and

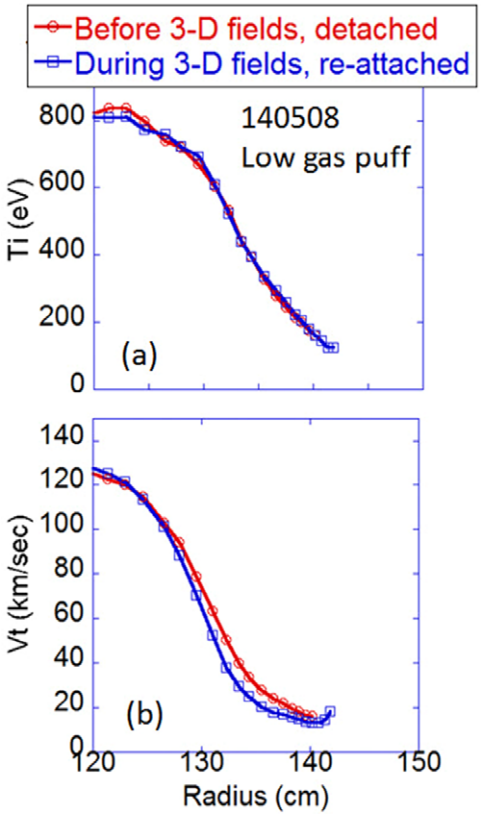

Figure 11. Pedestal T_i (*a*) and V_t (*b*) profiles before (red) and after (blue) the $n = 3$ fields application in the low gas puff case, during which divertor re-attachment was induced.

(*b*), is for the high gas puff and the lower row, (*c*) and (*d*), is for the low gas case. In the continued detachment (as described in section 4.1) with high gas puff, the pedestal T_e profile remains decreased before and after turning on the 3D field, so the applied 3D field has no effect on the T_e profile, figure 10(*a*). It is also seen in figure 10(*b*) that the USXR data for the edge channels continuously decrease. On the other hand, in the case of re-attachment, the pedestal T_e rises back up after the application of 3D fields, see figure 10(*c*). The increase is usually by ~100 eV and the edge soft x-ray data also shows increase, figure 10(*d*). As the pedestal n_e does not change significantly as explained above, this increase of edge USXR is attributed to the increase of pedestal T_e. It is noted that the T_i and V_t data in the pedestal region are not affected by the applied 3D fields even for the re-attachment case (see figure 11). This implies that the physical mechanism responsible for the divertor detachment and re-attachment is likely to be carried out by the change in electron thermal transport process. The observation of $T_{e,ped}$ increase and the unchanged $n_{e,ped}$ with the application of $n = 3$ fields is consistent with the previous result for the attached condition in NSTX without the use of lithium PFC coating referenced in section 4.2.1, reported in [6, 7, 18]. Note that we only used a minimal amount of lithium for the detachment experiment presented in this paper in order to keep ELMs, therefore these data should be compared to the case with no lithium in [18]. The observed $T_{e,ped}$ increase in case of re-attachment is found to be associated with the change in global parameters too. For example, the total radiation power

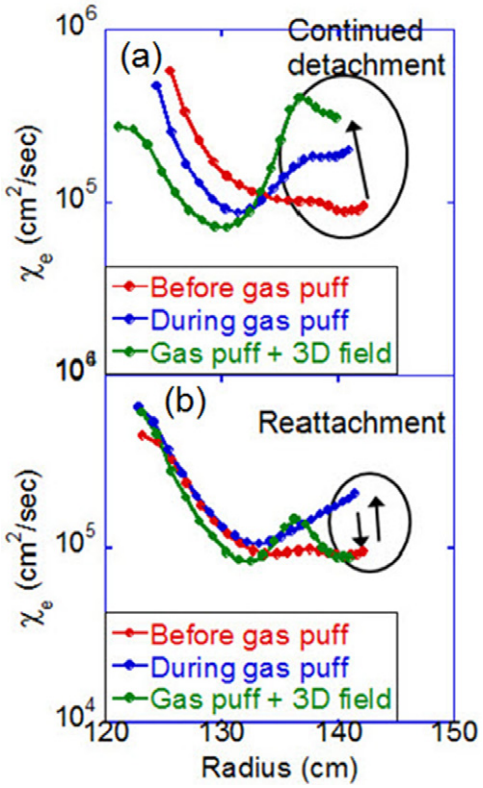

Figure 12. Evolution of pedestal χ_e profile from TRANSP modeling for (*a*) high and (*b*) low divertor gas puff with 3D fields applied later during the detached phase.

(P_{rad}) usually decreases during the detached phase in NSTX, but it rose back up when the plasma re-attached by 3D fields.

In an effort to explain how the observed $T_{e,ped}$ change was induced, a TRANSP [34] modeling was carried out for these discharges using the measured T_e and n_e profiles as input, and figure 12 shows the pedestal electron heat diffusivity (χ_e) profiles. The derivation of χ_e is based on the electron energy conservation equation as follows,

$$\frac{d}{dt}(n_e T_e) - \Delta \cdot \left(n_e \chi_e \frac{dT_e}{d\rho} \right) + \Delta \cdot (v_e T_e) = S_e, \qquad (1)$$

where ρ is the normalized toroidal flux, and v_e and S_e is the radial electron velocity and the source term, respectively. For the continued detachment case (with high gas puff), the pedestal χ_e continuously increases during the whole detachment and the later 3D field application phases (see figure 12(*a*)). It shows the same trend during the detachment phase, i.e. χ_e rises, in the low gas puff case, but the χ_e comes back down when the 3D fields are applied and the divertor re-attachment occurs (figure 12(*b*)). This result is consistent with the T_e profile data shown in figure 10. It is not yet understood why, under this condition, the 3D fields lead to reduced χ_e and higher T_e in the edge region.

One might interpret the dip in the T_e profile shown in figure 10 as a phenomenon associated with island formed in the respective radial location. However, when islands are formed in NSTX, it is usually accompanied by a flat spot at the radial location of the island in T_i and V_t profiles, measured by CHERS, as well as in the T_e and p_e profile [35, 36], but in the cases presented in this paper there is no such a spot in either the T_i or V_ϕ profile. Thus we believe the T_e drop here is not related to the island formation.

5. Summary and discussion

The use of 2D wide angle image data for the divertor footprints provides a tool to look into the impact of 3D fields more comprehensively, as compared to using the traditional 1D divertor flux profiles. It is noted that the spatial distribution of Li I visible light intensity agrees with heat flux profiles from the IR measurement. The new data confirms the previous result of $n = 3$ strike point splitting [11, 12] that the vacuum field line tracing (FLT) can effectively reproduce the splitting pattern, by allowing detailed comparison of 2D structure of each striation to that in the observed images. The size and relative spacing of striations are well reproduced for the toroidal and radial extents of the data studied in this work, although striations from vacuum FLT tend to extend in the toroidal direction slightly more (by 20°–30° at $r = 55$ cm) compared to the image data. The q_{95} dependence of the striation pattern, i.e. more and finer striations for higher q_{95}, also shows good agreement between the 2D image and the vacuum FLT data. The vacuum FLT in this work contains all three major contributions of intrinsic error fields ($n = 1$ and $n = 3$ components from the non-circularity of the PF5 coil and the $n = 1$ component from the TF coil). The phase locking of the ELM divertor footprints to the applied $n = 3$ fields is found to be related to the size of ELM. When the ELM energy loss is sufficiently small, e.g. $\Delta W_{ELM}/W_{MHD} < 4$–5%, the phase locking is well maintained over the whole period of ELM rise time, but it is lost at a later stage during the ELM rise time when the ELM size is large enough. This result suggests that at least a certain level of ELM mitigation would be necessary in order for the spatial distribution of ELM heat flux with 3D fields to be aligned with the footprint pattern generated by the imposed 3D fields. A re-attachment of partially detached divertor plasma by the applied 3D fields is observed from the IR heat flux profiles and the high-n Balmer line emission intensities, e.g. Balmer-10, but this can be avoided by sufficient divertor gas puff. Thomson and CHERS data show that T_e is essentially the only pedestal parameter that is related to the divertor condition; reduction of pedestal T_e ($\Delta T_{e,ped} \sim 100$ eV) was observed for detached condition and the re-attachment by 3D fields recovered the $T_{e,ped}$. A TRANSP modeling identified that the pedestal χ_e change is consistent with the observed T_e profile change during the detachment and re-attachment processes. The dependence of detachment behavior with 3D fields on several parameters, including mode number of perturbation fields, q_{95}, and pedestal collisionality, etc will need to be investigated in future experiments.

Acknowledgments

This work was supported by the US Department of Energy, contract numbers DE-AC05-00OR22725, DE-AC52-07NA27344 and DE-AC02-09CH11466. The authors

acknowledge the international collaboration with the IPP-Garching and the technical help from Dr A Herrmann for the use of THEODOR heat conduction code.

References

[1] Evans T E *et al* 2005 *Nucl. Fusion* **45** 595
[2] Evans T E *et al* 2006 *Nature Phys.* **2** 419
[3] Liang Y *et al* 2007 *Phys. Rev. Lett.* **98** 265004
[4] Suttrop W *et al* 2011 *Phys. Rev. Lett.* **106** 225004
[5] Jeon Y M *et al* 2012 *Phys. Rev. Lett.* **109** 035004
[6] Canik J M *et al* 2010 *Phys. Rev. Lett.* **104** 045001
[7] Canik J M *et al* 2010 *Nucl. Fusion* **50** 034012
[8] Evans T E *et al* 2005 *J. Phys.: Conf. Ser.* **7** 174
[9] Schmitz O *et al* 2008 *Plasma Phys. Control. Fusion* **50** 124029
[10] Jakubowski M W *et al* 2009 *Nucl. Fusion* **49** 095013
[11] Ahn J-W *et al* 2010 *Nucl. Fusion* **50** 045010
[12] Ahn J-W *et al* 2011 *Phys. Plasmas* **18** 056108
[13] Park J-K *et al* 2008 *Phys. Plasmas* **14** 052110
[14] Ahn J-W *et al* 2010 *Rev. Sci. Instrum.* **81** 023501
[15] McLean A G *et al* 2012 *Rev. Sci. Instrum.* **83** 053706
[16] Mordijck S *et al* 2010 *Nucl. Fusion* **50** 034006
[17] Alfier A *et al* 2008 *Nucl. Fusion* **48** 115006
[18] Canik J M *et al* 2012 *Nucl. Fusion* **52** 054004
[19] Maingi R *et al* 2009 *Phys. Rev. Lett.* **103** 075001
[20] Canik J M *et al* 2011 *Phys. Plasmas* **18** 056118
[21] Boyle D P *et al* 2011 *Plasma Phys. Control. Fusion* **53** 105011
[22] Maingi R *et al* 2012 *Nucl. Fusion* **52** 083001
[23] Herrmann A *et al* 1995 *Plasma Phys. Control. Fusion* **37** 17
[24] Scotti F *et al* 2012 *Rev. Sci. Instrum.* **83** 10E532
[25] Soukhanovskii V A *et al* 2003 *Rev. Sci. Instrum.* **74** 2094
[26] Soukhanovskii V A *et al* 2010 *Rev. Sci. Instrum.* **81** 10D723
[27] Stutman D *et al* 1999 *Rev. Sci. Instrum.* **70** 572
[28] LeBlanc B P *et al* 2003 *Rev. Sci. Instrum.* **74** 1659
[29] Bell R E *et al* 2010 *Rev. Sci. Instrum.* **81** 10D724
[30] Evans T E *et al* 2004 *Contrib. Plasma Phys.* **44** 235
[31] Menard J E *et al* 2010 *Nucl. Fusion* **50** 045008
[32] Soukhanovskii V A *et al* 2009 *Nucl. Fusion* **49** 095025
[33] Hirshman S P *et al* 2011 *Phys. Plasmas* **18** 062504
[34] Hawryluk R J 1980 *Physics of Plasmas Close to Thermonuclear Conditions* vol 1 ed B Coppi *et al* (London: Pergamon) p 19
[35] Menard J E *et al* 2005 *Nucl. Fusion* **45** 539
[36] Wong K L et al 2011 *Bulletin of the 53rd APS-DPP Annual Meeting (Salt Lake City, UT)* http://flux.aps.org/meetings/YR11/DPP11/all_DPP11.pdf